Nano Research

Open Access

Research Article

Bio-inspired microstructured Janus films enabling continuous 24 h thermoelectric energy harvesting

Honglin Li[1,§], Zhenmin Ding[2,§] ✉, Xin Li[3], Jiupeng Zhao[1], Yan Liu[2], Ana Sofia Oliveira Henriques Moita[4], Aleksandr Kuchmizhak[5,6] ✉, Yao Li[7] ✉, and Hongbo Xu[1] ✉

[1] School of Chemistry and Chemical Engineering, Harbin Institute of Technology, Harbin 150001, China
[2] Institute of Structured and Architected Materials, Liaoning Academy of Materials, Shenyang 110167, China
[3] College of Materials Science and Engineering, Northeast Forestry University, Harbin 150040, China
[4] IN+ - Center for Innovation, Technology and Policy Research, Instituto Superior Técnico, Universidade de Lisboa, Av. Rovisco Pais, Lisboa 1049-001, Portugal
[5] Far Eastern Federal University, Vladivostok 690922, Russia
[6] Institute of Automation and Control Processes (IACP), Far Eastern Branch of Russian Academy of Sciences, Vladivostok 690091, Russia
[7] Center for Composite Materials and Structure, Harbin Institute of Technology, Harbin 150001, China
[§] Honglin Li and Zhenmin Ding contributed equally to this work.

Cite this article: *Nano Research*, **2026**, *19*, 94908403. https://doi.org/10.26599/NR.2026.94908403

ABSTRACT: Radiative cooling technology shows promise for improving thermoelectric generator (TEG) efficiency, but challenges in hot-end design and model validation remain. To address this, a Janus moth-eye-inspired device was developed, leveraging microstructure-enhanced absorption/emission. This device combines a SiO_2 radiative cooler with a radiative Si photothermal absorber in a synergistic configuration. When integrated into a commercial TEG for gradient-based power generation, the Janus composite demonstrated exceptional performance: a peak output voltage of 108 mV, an average daytime voltage of 70 mV under summer daylight conditions, and an output power density reaching 41.5 μW/cm². This study systematically investigates the key parameters of the Janus structure and their impact on the voltage output. Furthermore, it experimentally validates the efficacy of both the SiO_2 radiative cooler and Si photothermal absorber in boosting TEG performance. These findings establish a foundation for future research on stable, rigid biomimetic microstructured thin films for advanced thermoelectric applications.

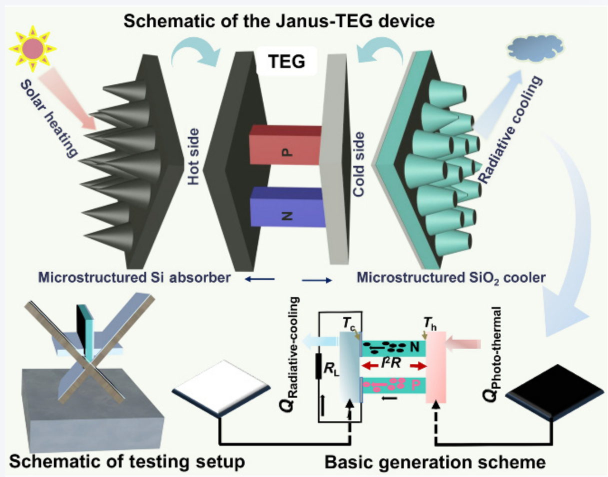

KEYWORDS: Janus structure, bioinspired microstructures, radiative cooling, solar heating, thermoelectric power generation

1 Introduction

Amidst the rapid global economic growth today, energy, as a vital driver of societal progress, continues to experience escalating demand, paralleled by mounting pressures for environmental conservation. Confronted with global challenges, such as the depletion of fossil fuels and intensifying climate change [1–3], the quest for efficient, clean, and sustainable energy conversion and utilization technologies has emerged as a shared responsibility and mission for all humanity [4]. Thermoelectric generator (TEG) technology [5], with its unique advantage of directly converting ubiquitous thermal energy into electricity, stands as a green and low-carbon energy solution that is gradually gaining prominence in scientific research and industry, showcasing immense application potential and a vast market prospect [6–8]. Given the environmental friendliness of the thermoelectric effect, advances in high-performance thermoelectric materials and devices are now

Received: October 20, 2025; **Revised:** December 12, 2025
Accepted: January 5, 2026

✉Address correspondence to Zhenmin Ding, zmding@lam.ln.cn; Aleksandr Kuchmizhak, alex.iacp.dvo@mail.ru; Yao Li, yaoli@hit.edu.cn; Hongbo Xu, iamxhb@hit.edu.cn

widely regarded as a pivotal frontier in sustainable energy harvesting [9, 10].

Leveraging the Seebeck effect [11], TEG systems generate power through temperature gradients, with performance heavily dependent on the thermal differential between hot and cold junctions. Current research strategies focus on enhancing this gradient—either by elevating hot-side temperatures using industrial waste heat [12], body heat [13], solar energy [14], etc., by reducing cold-side temperatures via active or passive cooling. However, these approaches face inherent limitations: Industrial waste heat systems are often complex and costly [15], body heat yields insufficient thermal gradients [16], while active cooling methods (e.g., water/air cooling) incur parasitic energy losses [17–19]. Passive radiative cooling, which exploits the 8–13 μm atmospheric window to dissipate heat into space, has emerged as a viable alternative [20–22], yet its standalone application fails to maximize TEG output. Crucially, optimizing TEG performance requires synergistic integration of hot-side photothermal heating and cold-side radiative cooling—a challenge that remains unresolved.

Recent advances in hybrid TEG systems highlight this potential. In particular, pioneering work by Mu et al. demonstrated radiative cooling-driven power generation, achieving 4 °C temperature difference and 0.18 mV electrical output [23]. Raman et al. [24]. subsequently demonstrated nighttime device operation under light-emitting diode (LED) illumination, while Fan et al. [25]. improved device performance through material optimization, specifically highlighting the critical role of selective emitters. Concurrently, Zhao et al. [26]. established theoretically that maximum power output occurs when internal and external resistances are not equal. Critically, enhancing TEG power output requires synergistic hot-side photothermal heating alongside cold-side radiative cooling—not radiative cooling alone. However, existing designs predominantly rely on ambient air as the hot-side heat source, significantly constraining power output [27]. Moreover, the gap between theoretical models and experimental validation hinders progress toward practical deployment [28, 29].

To address these challenges, this study introduces a biomimetic Janus-structured metamaterial device that synergistically combines a subwavelength-engineered quartz (SiO_2) radiative cooler with a silicon (Si) photothermal absorber [30, 31]. Innovative Janus design of the device achieves two key breakthroughs for efficient thermoelectric energy harvesting. First, by integrating a SiO_2 radiative cooler and a Si solar light absorber, we have created a dual-mode cold/hot interface that generates steep thermal gradients to increase the power output of conventional TE systems that rely on ambient air. Second, rigorous experimental validation of the modeled designs, which show improved device performance, bridges the gap between simulations and real-world performance, establishing scalable design principles for high-efficiency TEG systems. Our work not only advances the fundamental understanding of hybrid photothermal-radiative cooling TEG systems but also provides a practical pathway toward their commercialization. Through continued optimization, this technology holds significant promise for sustainable energy applications in an increasingly resource-constrained world.

2 Results and discussion

The Seebeck effect [32, 33] dictates that even modest increase in the temperature difference across a thermoelectric device will not sufficiently enhance the device's voltage output capability. Traditional approaches focusing solely on optimizing either the hot or cold sides of TEG systems inherently limit further improvements in power generation efficiency. To address this constraint, we developed a Janus-like composite TEG device (Fig. 1(a)). This device features a thermoelectric element as its core substrate, equipped with a Si photothermal plate at the hot side and a SiO_2 radiative cooling plate at the cold side. Opposite-functioning heat-absorbing and heat-radiating films are integrated onto both sides. By leveraging the asymmetry in thermal management across the dual surfaces, the temperature difference across the thermoelectric element is amplified, ultimately enhancing power generation efficiency. In the ideal case, both sides of the TEG should possess the spectral characteristics shown in Fig. 1(b), with the maximal absorption in the solar band (0.25–2.5 μm) and nearly zero infrared (IR) emissivity at wavelengths above 2.5 μm, thus ensuring the efficient solar heating (top panel in Fig. 1(a)). Zero solar absorption combined with maximal IR emissivity within the atmospheric window (8–13 μm) and zero emissivity in the remaining infrared bands represent the conditions ensuring efficient radiative cooling performance (bottom panel in Fig. 1(a)).

The integration of Si photothermal plate in solar heating mode and SiO_2 radiative cooling plate in the cooling mode at both sides of the TEG can maximize the temperature difference of the TEG and improve its power generation capability. The left two panels on Fig. 1(c) provide scanning electron microscopy (SEM) and optical images of the SiO_2 radiative cooling plate featuring the surface morphology in the form of an array of truncated micro-cones with a top and base diameter of ~ 0.6 and 1.2 μm, respectively. As shown in Fig. 1(d) (red curve), such design allows for achieving exceptional radiative cooling performance with solar-band absorption below 2.9% and high atmospheric-window emissivity of 94.9%. The detailed fabrication protocol and basic characterization of the SiO_2 micro-cone surfaces can be found elsewhere [34]. Right two panels of Fig. 1(c) reveal the general morphology and optical appearance of the Si photothermal plate composed of sharp micro-cones. Finite-difference time-domain (FDTD) simulations were first carried out to optimize the micro-cone morphology in terms of solar band absorption efficiency achieved for a micro-cone height/base around 1/0.5 μm and a cone angle of 28° (see Fig. S1 and Supplementary note 1 in the Electronic Supplementary Material (ESM)). The mask-assisted reactive etching procedure was then parametrically optimized to realize the modeled design over the surface of N-type silicon wafer (Fig. S2 in the ESM). Advanced performance of the optimized structure was then confirmed through systematic studies involving optical spectroscopy, outdoor tests of the light-to-heat conversion performance, and net heating power assessments (Figs. 1(e) and 1(f) and Supplementary note 1 in the ESM). These systematic tests approved the superior visible absorption ($\alpha_{0.25-2.5}$ = 0.95) and low infrared emissivity ($\varepsilon_{2.5-25}$ = 0.45) of the designed microstructured Si plate (Fig. 1(d)), strong heating capacity calculated at different non-radiative losses with an excellent heating power of 756.22 W/m² (Fig. 1(e)). All these characteristics, together with the improved solar light-to-heat conversion efficiency of the microstructured Si, exhibiting a temperature increase of ~ 28.7 °C above the ambient temperature level in the outdoor tests (Fig. 1(f) and Fig. S3 in the ESM), justify the developed design for TEG applications.

To further assess the photothermal performance of the microstructured SiO_2 and Si plates, we carried out indoor tests with

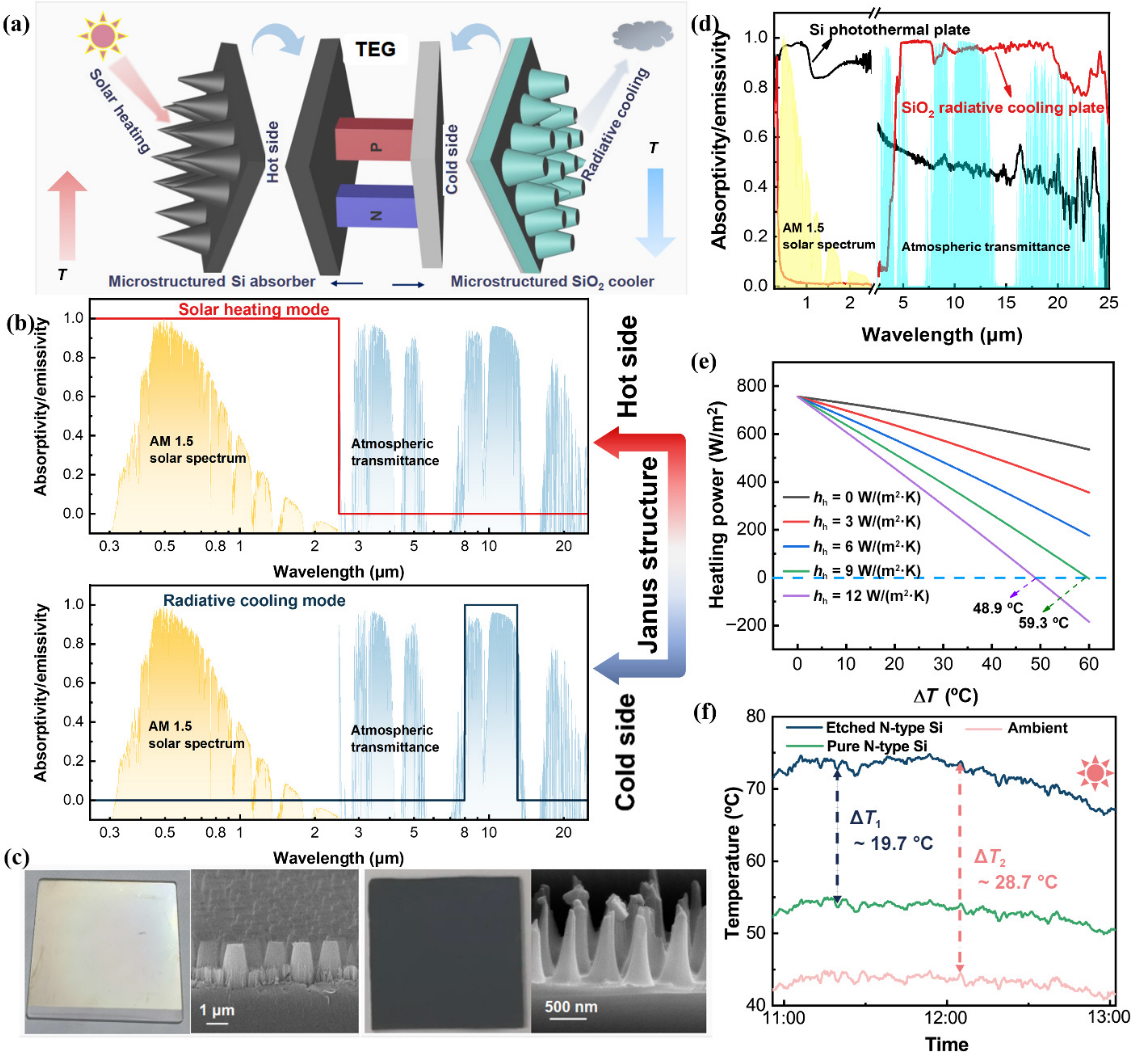

Figure 1 Microstructured Janus TEG device. (a) Schematics of the TEG device containing microstructured Si layer for enhanced solar light absorption and microstructured SiO_2 layer for radiative cooling at the hot and cold sides of the device. (b) Idealistic spectral characteristics of the microstructured layers on both sides of Janus TEG, allowing maximal solar light heating (top panel) and radiative cooling (bottom panel) performance. AM 1.5 solar spectra and atmospheric transmittance windows are also indicated on both panels for visual guidance. (c) Optical and SEM images of the optimized SiO_2 (left panels) and Si (right panels) microstructured layers realized over cold and hot sides of the designed TEG device. (d) UV–vis–NIR absorptivity and emissivity of the optimized SiO_2 (red curve) and Si (black curve) microstructured TEG layers. (e) Net heating power of the microstructured Si layer of the TEG calculated at different hh values. (f) Outdoor temperature curves of pristine and microstructured N-type Si measured during the daytime. Variation of the ambient temperature is also presented in the figure.

a 0.5 kW/m² xenon lamp imitating solar exposure. A series of IR thermal images in Fig. 2(a) demonstrates elevated temperature difference between the microstructured SiO_2 and Si plates under accumulated light exposure. The former exhibits low solar band absorption, with the average temperature remaining almost constant throughout the exposure period. In a sharp contrast, the microstructured Si demonstrates outstanding light-to-heat conversion performance with its temperature reaching 51 °C within 150 s of the xenon lamp exposure. Comparative outdoor tests performed using TEG1-127 benchmark plate also confirmed the general deductions made (Fig. 2(b)), demonstrating the temperature difference between microstructured Si and SiO_2 plates reaching 21.7 °C on the IR images. Furthermore, the studied heating dynamics of both plates monitored by a thermocouple under xenon lamp exposure confirmed the IR imaging results showing the microstructured Si reached 52.5 °C in less than 200 s (Fig. 2(c)). Next, more detailed outdoor tests were also conducted to further examine the heating and cooling capabilities of the photothermal and the radiative cooling TEG layers. Outdoor temperature measurements were conducted using the setup shown in Fig. 2(d), where an aluminum foil-wrapped foam box effectively reduces heat transfer from the external environment and solar radiation heating, and a polyethylene (PE) film encloses the box to prevent heat convection with the air. The measured temperature and temperature difference curves are shown in Figs. 2(e) and 2(f), respectively. As can be seen, the average temperature at the surface of the microstructured Si plate was 42.6 °C, with the maximum value reaching 58 °C (25.2 °C higher than the ambient temperature at midday hours). Under the same conditions, the average temperature drop of the SiO_2 radiative cooling plate was about 6 °C, with its maximal value exceeding 9 °C. The maximum temperature difference between the microstructured Si and SiO_2 plates was 34.3 °C, substantiating their potential for TEG applications to provide stable and continuous output voltage.

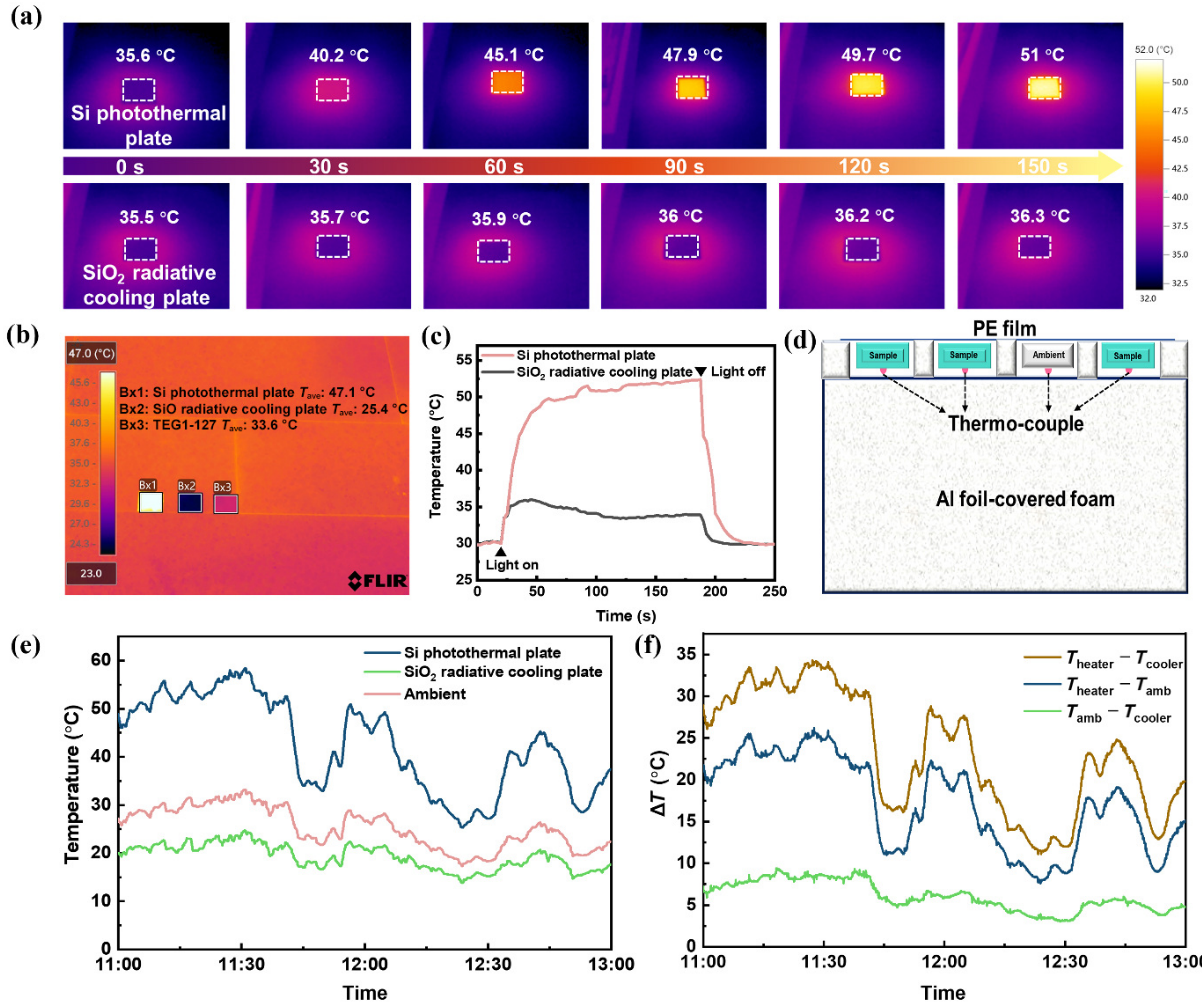

Figure 2 Heating/cooling performance of microstructured Si and SiO_2 plates. (a) A series of IR images showing temperature variations of both plates exposed to xenon lamp at different times. (b) IR image comparing light-to-heat conversion performance of microstructured Si and SiO_2 plates and bare TEG1-127 benchmark device under outdoor sunlight exposure. (c) Temperature variation of microstructured Si and SiO_2 plates under xenon lamp exposure (0.5 kW/m²). (d) Schematics of the device for outdoor temperature testing. (e) Variation of the temperatures of microstructured Si (T_{heater}) and SiO_2 plates (T_{cooler}) during their outdoor testing at midday hours, and (f) temperature differences ($T_{heater} - T_{cooler}$, $T_{heater} - T_{amb}$, and $T_{amb} - T_{cooler}$) assessed with respect to each other and an ambient temperature (T_{amb}).

We subsequently explored the temperature difference and voltage output at the two sides of the designed bare TEG (marked as bare-mode in Figs. 3(a)–3(c)), as well as the same device containing either microstructured Si (marked as SH-mode) or SiO_2 plates atop (marked as RC-mode). The schematic diagram for outdoor TEG performance testing is presented in Fig. S4 in the ESM, emphasizing the identical orientation of the devices in all tested modes. Detailed description of the measurement protocol is provided in Supplementary note 2 in the ESM.

Figures 3(d)–3(f) compare the temperature variation at both the cold and the hot sides of the TEG for mentioned outdoor testing modes. The corresponding temperature difference and modulation of solar irradiance conditions (green-shaded area) during the monitored period, are also provided. As can be seen, for nearly similar average solar irradiance around 600 W/m², the hot-end temperature for the bare-mode was maintained within 20–40 °C, which is notably lower than the temperature observed for the device tested in SH-mode, where temperatures above 50 °C can be observed. In contrast, the device tested in RC-mode demonstrates generally lower temperatures as compared to those for bare TEG. Figure 3(g) provides the data on the difference between the temperatures of the hot and cold sides of the devices tested in different operation modes. Almost zero difference can be identified for the bare device, while values of 0.7 and 1.0 °C are obtained for the device tested in the SH-mode and RC-mode, respectively. By simultaneously monitoring the output voltage of the corresponding TEG (Fig. 3(h)), one can reveal improved power generation capacity of the devices operated in both solar heating and radiative cooling regimes. In particular, the average voltages generated at SH- and RC-modes were 21.9 and 15.5 mV, respectively (Fig. 3(i)), yielding a 3.1- and 2.2-fold increase as compared to those for the bare device. Simultaneously, voltage output performance and temperature were tracked under a solar simulator for three distinct modes. Figures S5(a)–S5(d) in the ESM record the temperatures at the hot and cold sides of the TEG and the temperature difference between the two sides. Consistent with outdoor trends, the hot-side temperature in SH-mode was significantly higher than that in bare-mode, while the temperature in RC-mode was slightly lower than that in bare-mode. Regarding temperature gradients, the temperature differences under bare-mode, SH-mode, and RC-mode testing were 0.6, 5.6, and 2.1 °C, respectively. Monitoring the output voltage across the TEG terminals (Figs. S5(e) and S5(f) in

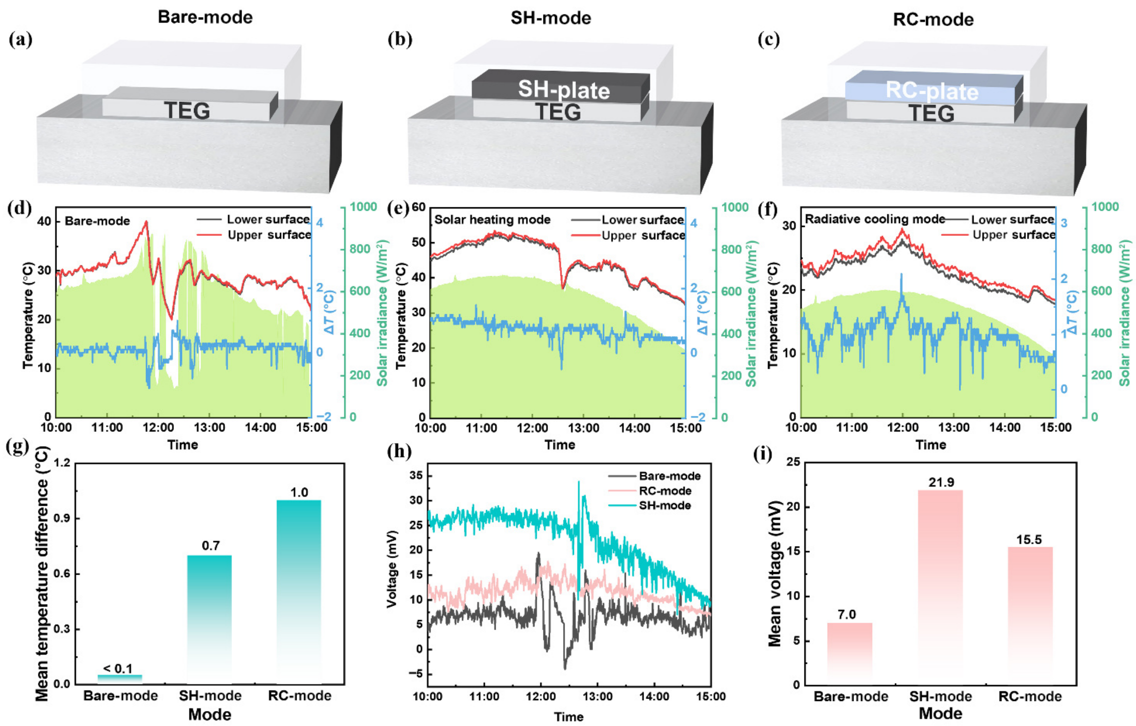

Figure 3 ((a)–(c)) Schematics illustrating different TEG operation modes, including (a) bare device mode (bare-mode), (b) solar heating mode (SH-mode), and (c) radiative cooling mode (RC-mode). ((d)–(f)) Daytime variation of the hot-side (red curves) and cold-side (black curves) temperatures, corresponding temperature difference (blue curves), and solar irradiance conditions (green-shaded area) measured under outdoor tests at different modes of the TEG device operation. (g) Difference between the temperatures of cold and hot sides of the TEG averaged over daytime monitoring period for different operation modes. (h) Variation of the TEG voltage and its averaged value (i) upon outdoor test for different modes.

the ESM) yielded results consistent with outdoor testing. The TEG output voltages in SH-mode and RC-mode were 39.2 and 10.4 mV, respectively, 8.3 and 2.2 times higher than the bare-mode output voltage. Both modes demonstrated enhanced power generation performance.

The demonstrated results highlight the ability of both microstructured plates to boost the voltage output of the TEG device through enlarged temperature difference [35]. Notably, SH-mode provides stronger positive effect on the TEG performance, which can be attributed to the higher operation temperatures that are beneficial for the improved voltage output [36–38]. To improve the thermoelectric conversion efficiency, additional theoretical studies were carried out, as outlined in Supplementary note 3 in the ESM. By enhancing the emissivity of radiative coolers to boost cooling power and integrating them with TEGs that have high figure of merit (ZT) values, the overall performance of thermal-to-electrical energy conversion systems can be significantly improved, guiding the TEG design optimization.

Leveraging radiative cooling capability of the microstructured SiO_2 plate and photothermal conversion performance of the microstructured Si plate, a hybrid Janus TEG system has been developed. The general device scheme is shown in Figs. 4(a) and 4(b), where two silver mirrors were fixed on a vertical wooden support frame. Commercial TEG device was positioned vertically in the middle of two mirrors with the microstructured Si and SiO_2 plates tightly attached to the opposite sides of the device. The photograph of the test chamber is presented in Fig. S6 in the ESM, which is covered with insulating foam and a high-transmittance PE film to minimize the impact of thermal conduction and convection, ensuring the accuracy and stability of the test results. Driven by thermally induced carrier concentration gradient on the hot side of the TEG, the holes and electrons diffuse toward its cold side, thus forming a potential difference at the low-temperature open circuit side. Notably, heat generated upon solar energy absorption by the microstructured Si plate continuously diffuses towards the radiative cooler side, resulting in a temperature difference across the TEG that is lower as compared to the maximum value (Fig. 2(f)). TEG performance is largely dependent on the solar irradiance, which is generally season-dependent. In this respect, we next measured the daytime voltage variation of the Janus TEG across different seasons. In particular, during a typical day in spring (Fig. 4(c)), the maximal solar irradiance (observed between 10:00 and 12:00) continuously drops with time, yielding in a similar trend of the voltage variation with its average value about 21.8 mV. In contrast, despite a certain modulation of the solar irradiance during the testing summer day (Fig. 4(d)), the average voltage of the developed TEG was as high as 70.0 mV, with its maximum value reaching 108 mV. Moderate (38.2 mV) and low (6.7 mV) voltage output was obtained upon device testing during typical autumn and winter days, generally reflecting the seasonal variations of the solar irradiance (Figs. 4(e) and 4(f)). Summing up the seasonal performance of the Janus TEG, the average daytime output voltage is shown in Fig. S8 in the ESM. Summer is indeed optimal time for device operation with about two- and ten-fold increase over the average voltage output as compared to the values obtained during the autumn and winter days, respectively. Additionally, the device operation was attested during the nighttime at different seasons (Fig. 4(g)), where similar trends with the maximal (minimal) performance achieved during summer (winter) days were identified. Analysis of the measured data allows us to estimate the seasonal nighttime variation of the

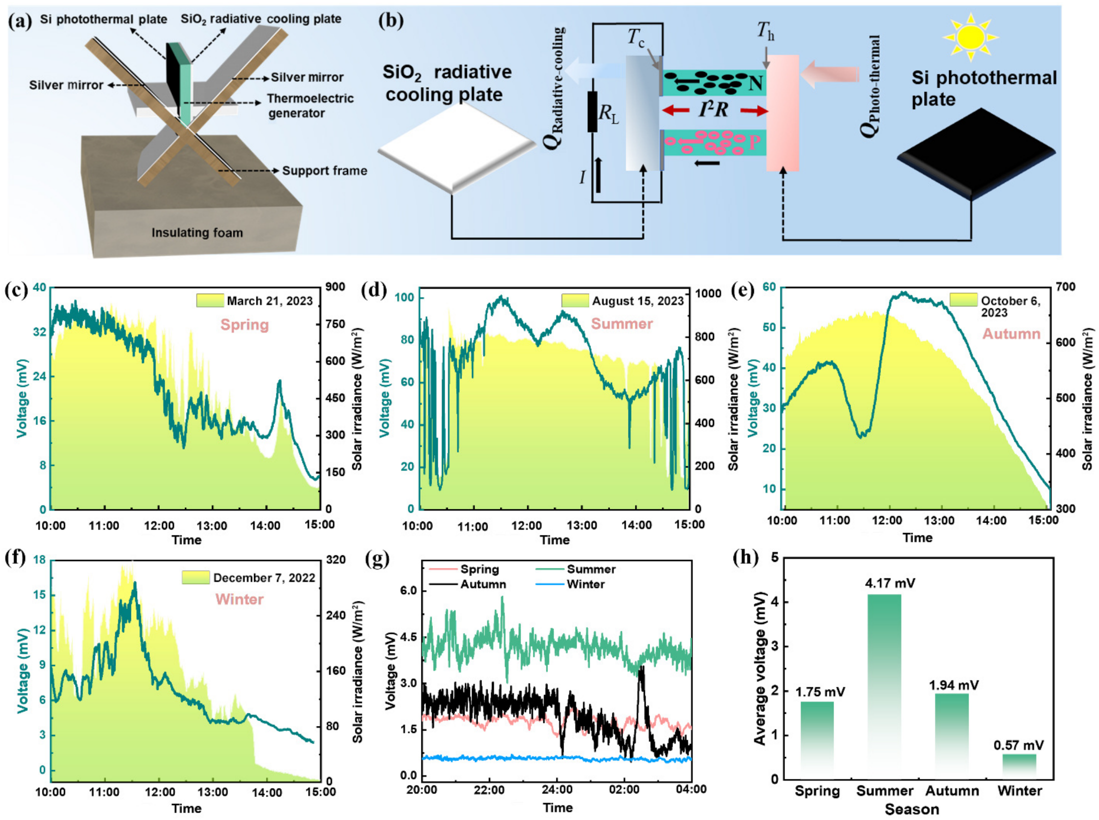

Figure 4 Seasonal outdoor performance of the Janus TEG. (a) Schematics of the developed device and (b) its basic generation scheme. ((c)–(f)) Variation of the output voltage of the Janus TEG (curves) and solar irradiance (green-shaded areas) during the representative days in (c) spring, (d) summer, (e) autumn, and (f) winter. (g) Representative nighttime voltage variation in the developed device and (h) seasonal averaged voltage values for nighttime operation.

average TEG voltage shown in Fig. 4(h), revealing average values of approximately 1.8, 4.2, 1.9, and 0.6 mV for spring, summer, autumn, and winter, respectively.

To validate the all-weather power generation capability of the composite power generation device, a 24 h outdoor voltage test was conducted, as shown in Fig. S9 in the ESM. Throughout the entire test period, the composite power generation device consistently maintained voltage output, achieving a peak voltage exceeding 55 mV. Even at night (18:00–6:00), without the solar heating on the hot side to increase the temperature difference, under the all-weather radiative cooling drive on the cold side, it could still generate an average voltage of 1.9 mV. Regardless of the season, the nighttime device performance drops significantly as compared to the daytime values, as the hot side of the Janus TEG device relies on heat absorption empowered by microstructured Si plate during the day. Conversely, in the absence of strong photothermal effect during the nighttime, the temperature difference between cold and hot sides is mainly driven by radiative cooling effect. At the same time, this temperature difference (as well as device operation temperature) is considerably lower than that for the daytime, resulting in decreased thermoelectric efficiency of the Janus TEG. This aligns well with the abovementioned discussions, which established a positive correlation between the voltage generation and both the operating temperature and the magnitude of the temperature difference between the hot and cold sides of the device (Fig. 3).

Figure 5 summarizes the results of the Janus TEG testing in an open system, i.e., without the protective PE film cover. Variation of the solar irradiance as well as temperatures of the cold and hot junctions of the device monitored during the testing day (October 11, 2023) are shown in Figs. 5(a) and 5(b). The data indicate temperature variation between 15 and 29 °C, markedly lower compared to the value measured in the closed system. These temperature variations largely follow the solar irradiance profile, yet the removal of the PE cover exposes the TEG to environmental thermal convection, resulting in an average diurnal temperature difference of about 2.7 °C at the maximal value of 8.6 °C, significantly higher than those achieved with either a standalone microstructured Si plate (0.7 °C) or a standalone microstructured SiO_2 plate (1.0 °C). Figure 5(c) compares the diurnal voltage variation for TEG1-127 and TEG1-199 benchmark devices empowered by applying the developed Janus design, where the average voltages of 30.6 and 11.6 mV can be identified for both devices, respectively. Power generation performance of the Janus TEG is presented in Figs. 5(e) and 5(f), where the maximal value was observed at an ambient temperature of approximately 19 °C, with a hot junction temperature of 32.6 °C, yielding a temperature difference of 4.4 °C. Under these conditions, the device exhibits a voltage of 54.0 mV and a current of 12.3 mA, corresponding to the output power of 664.2 μW or 41.5 μW/cm^2, considering 16 cm^2 device active area. These results underscore the superior power generation capabilities of the open-system Janus TEG, propelling the practical application of the designed thermoelectric devices.

Finally, Table S1 in the ESM compares the key characteristics (temperature difference, output voltage, and output power/power density) of the recently reported state-of-the-art TEGs empowered by radiative cooling technologies. Among them, commercial TEGs with 127 N–P semiconductor pairs have been frequently employed as experimental benchmarks; yet, the demonstrated devices

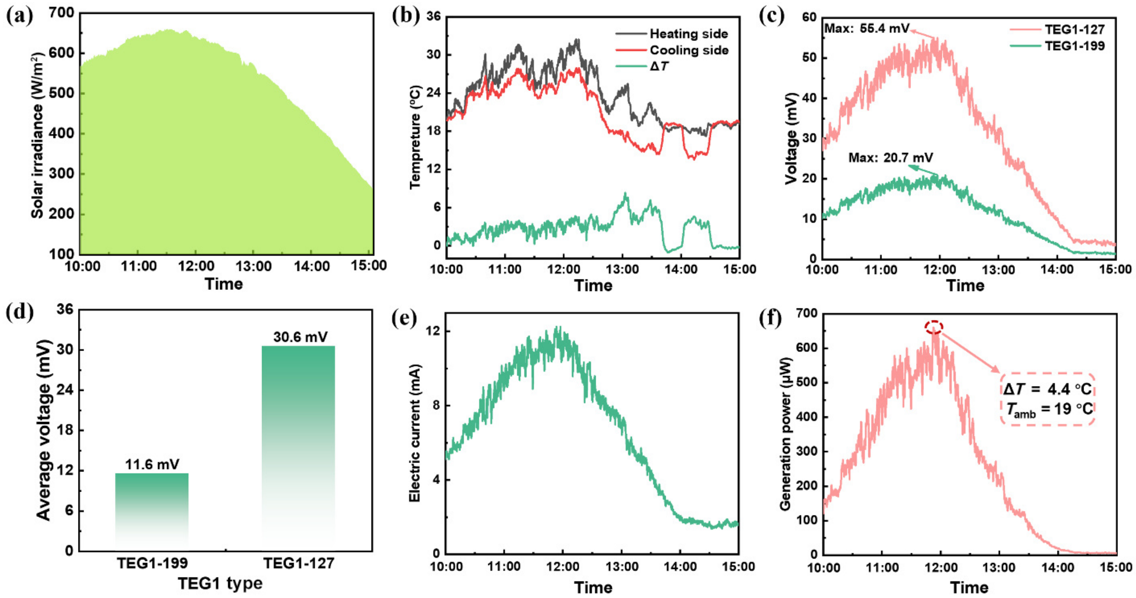

Figure 5 Outdoor performance of the Janus TEG under open system conditions. (a) Daytime variations of the solar irradiance. (b) Hot-side and cold-side TEG temperatures (black and red curves) and their difference (green curve). (c) Daytime variations of the voltage of the TEG1-127 and TEG1-199 devices and (d) their average daytime performance. (e) Daytime electric current variation in the Janus TEG and (f) electrical power calculated using the current and voltage data of the device.

generally struggle to reach a temperature difference above 5 °C. In contrast, the developed Janus TEG demonstrates outstanding performance with a temperature difference of up to 8.9 °C, a voltage output up to 108 mV, resulting in superior power density generated.

3 Conclusions

Integrating radiative cooling technologies into traditional TEG systems necessitates overcoming key challenges, particularly in optimizing the hot-side component design and enhancing overall system performance. Here, we suggested and validated an innovative Janus-inspired biomimetic microstructured device that harnesses the principle of nanostructure-empowered absorption/emission. This device synergistically integrates microstructured SiO_2 and Si plates acting as a radiative cooler and a photothermal converter, respectively. The resulting Janus TEG exhibited optimal performance during the summer season, with an average daytime voltage of 70.0 mV and a peak voltage reaching 108 mV, surpassing the performance observed during spring, autumn, and winter seasons. Notably, the nighttime voltage was also highest during summer. Under open-system conditions, the power generation capabilities of the composite TEG were markedly enhanced, achieving state-of-the-art characteristics with a maximum daytime voltage of 55.4 mV, a power output of 664.2 μW, and a power density of 41.5 μW/cm². This study offers new insights into hot-side component design and validation. Moreover, it delivers a solid technical foundation and experimental evidence to accelerate the commercialization and widespread adoption of TEG technologies.

4 Experimental

4.1 Materials

SiO_2 and Si substrates were acquired from Aladdin. All additional chemicals, inclusive of nitric acid (HNO_3), silver (Ag), ethanol (C_2H_5OH), and acetone (CH_3COCH_3), were procured as analytical-grade reagents from Tianjin Tianli Chemical Reagents Ltd. Experimental gases, such as argon (Ar, 99.99% purity), oxygen (O_2, 99.99% purity), nitrogen (N_2, 99.99% purity), sulfur hexafluoride (SF_6, 99.99% purity), and trifluoromethane (CHF_3, 99.99% purity), were sourced from Harbin Liming Gas Co., Ltd. TEG (composed of n-type and p-type semiconductor pairs made of Bi_2Te_3 sandwiched between hot and cold plates) were provided by Suqian Qingdou E-commerce Co., Ltd.

4.2 Fabrication of microstructured Si and SiO_2 plates

Microstructured Si plates were prepared by reactive ion etching (RIE) performed through the self-assembled layer of polystyrene (PS) microspheres. The detailed process is illustrated in Fig. S12 in the ESM, and the relevant technical details can be found in our previous studies [39]. PS microspheres with a diameter of approximately 500 nm were selected. During the RIE process, SF_6 and CHF_3 served as the etching gases for Si, while O_2 was used to remove the mask. To prepare the optimized microstructured Si plate, the gas flow ratio of SF_6:CHF_3:O_2 was set to 20:10:15. FDTD simulations were carried out to model the optical response of the microstructured surfaces and optimize micro-cone geometry towards maximal photothermal performance. Simulation details and optimization results are provided in Supplementary note 1 in the ESM and figures therein. Similar to the fabrication strategy for microstructured Si plates, the fabrication of microstructured SiO_2 plates also utilized FDTD to optimize the microstructure array on the SiO_2 surface. Subsequently, Ag spheres formed by annealing vacuum-deposited Ag metal films served as masks for RIE. CHF_3 and Ar were employed as etching gases with a gas flow ratio of 20:8 and an etching duration of 30 min. The etched samples were immersed in nitric acid solution to remove residual Ag. Finally, a metallic Ag layer was deposited on the cleaned sample backside to serve as a reflective substrate. The entire fabrication and design process of the microstructured SiO_2 radiative cooler was based on our previous research work, specifically the Experimental section in Ref. [34].

4.3 Measurements and characterizations

The microstructure of the microstructured Si and SiO_2 plates was characterized using a SEM (Sigma 300, Zeiss, Germany) operated at an acceleration voltage of 10–20 kV. Ultraviolet–visible–near infrared ray (UV–vis–NIR) spectral reflectance was measured using a UV–vis–NIR spectrophotometer (Lambda-1050+, PerkinElmer, USA) across the wavelength range of 0.25–2.5 μm, employing an integrating sphere with a $BaSO_4$ baseline reference. Mid-infrared spectral emittance of the samples was determined using a Fourier transform infrared spectrometer (Vertex 70, Bruker, Germany) equipped with an A562 integrating sphere, covering the wavelength range of 2.5–25 μm. Infrared thermography was conducted using a Fluke Tix660 infrared camera (Fluke Corporation, USA) to capture thermal images of the microstructured Si and SiO_2 plates at different temperatures.

4.4 Thermoelectric power generating performance test

We utilized commercially available TEG modules, which were classified into different models based on the number of series-connected P–N semiconductor pairs, such as TEG1-127, TEG1-199, and TEG1-241. According to previous research [40], these commercial TEGs had to be mounted on a flat surface, particularly at the cold side. The height difference of the mounting surface should not exceed 20 μm, and the applied pressure should be less than 12–15 kg/cm^2. For the TEG1-127-1.4-1.0 power generation module, the "127" denoted the number of generating units in this component, which corresponded to 127 pairs of semiconductors and 254 PN junctions connected in series. Table S2 in the ESM presents the dimensional parameters of these three commercial TEG modules. A preliminary screening of indoor testing was conducted on the aforementioned commercial TEG modules, with the specific testing setup shown in Fig. S10 in the ESM. The experiment utilized a heating stage to provide a stable heat source. The TEG modules were connected to a multimeter with recording capabilities through two wires to record real-time changes in voltage, current, and other parameters. By connecting thermocouples to the hot and cold sides of the TEG modules and linking the other sides of the thermocouples to a multi-circuit temperature measuring instrument, the temperature variations at the cold and hot sides of the TEG devices were monitored and recorded in real-time. Therefore, this setup allowed for the acquisition of voltage data at different temperatures. The indoor voltage test results of the specific TEG plate are shown in Fig. S11 and Supplementary note 4 in the ESM. TEG1-127 produced average voltages of 26.3, 65.3, and 105.3 mV under the heating conditions of 30, 40, and 50 °C, respectively, which was almost triple the generating capacity of the TEG1-199 of the same area, and was comparable in performance to the larger-sized TEG1-241. Based on the test results, TEG1-127 was mainly selected as the main research object for the outdoor performance exploration, while TEG1-199 was used as the control experiment to facilitate a more accurate evaluation of its performance.

Electronic Supplementary Material: Supplementary material (additional SEM images, visible absorptivity spectra, schematic diagrams of device and the preparation process for Si microstructured photothermal sheet, additional data of power generation performance, comparison table of power generation performance with commercial thermoelectric power generation tablets, table of the size parameters of different thermoelectric generation tablets, and Supplementary notes 1–4) is available in the online version of this article at https://doi.org/10.26599/NR.2026.94908403.

Data availability

All data needed to support the conclusions in the paper are presented in the manuscript and the Electronic Supplementary Material. Additional data related to this paper may be requested from the corresponding author upon request.

Acknowledgements

This work is granted by the National Key R&D Program of China (No. 2022YFB3902704), the National Natural Science Foundation of China (No. 5247020620), International Research Programs and Strategic Innovative Programs of National Key R&D Program of China (No. 2024YFE0105500), and the Natural Science Foundation of Heilongjiang Province (No. LH2023E034).

Declaration of competing interest

All the contributing authors report no conflict of interests in this work.

Author contribution statement

J. P. Z. and H. B. X. present a conceptualization. A. K. and Y. L. (Yao Li) provide the resources and funding acquisition. Z. M. D. and H. L. L. launched an investigation and finished writing the original draft. X. L., Y. L. (Yan Liu), and A. S. O. H. M. revised the first draft. All the authors have approved the final manuscript.

Use of AI statement

None.

References

[1] Kotz, M.; Levermann, A.; Wenz, L. The economic commitment of climate change. *Nature* **2024**, *628*, 551–557.

[2] Manghwar, R.; Selvaraj, J.; Abd Rahim, N.; Kumar, L.; Khoharo, H. Global advancements of solar thermoelectric generators application, limitations, and prospects: A comprehensive review. *Appl. Therm. Eng.* **2024**, *257*, 124231.

[3] Afifa; Arshad, K.; Hussain, N.; Ashraf, M. H.; Saleem, M. Z. Air pollution and climate change as grand challenges to sustainability. *Sci. Total Environ.* **2024**, *928*, 172370.

[4] Yu, L.; Xi, Z. Y.; Li, S.; Pang, D.; Yan, H. J.; Chen, M. J. All-day continuous electrical power generator by solar heating and radiative cooling from the sky. *Appl. Energy* **2022**, *322*, 119403.

[5] Lv, S.; Zhang, B. L.; Ji, Y. S.; Ren, J. W.; Yang, J. H.; Lai, Y.; Chang, Z. H. Comprehensive research on a high performance solar and radiative cooling driving thermoelectric generator system with concentration for passive power generation. *Energy* **2023**, *275*, 127390.

[6] Lv, S.; Deng, J. C.; Feng, M. Q.; Zhan, Z. P.; Xie, S. Z.; Deng, Y. R. Ultra-high electrical efficiency scalable RC-TE devices utilize renewable radiation energy from the sun and cold outer space. *Sol. Energy Mater. Sol. Cells* **2024**, *278*, 113154.

[7] Liu, W. Y.; Sun, S. M.; Zhu, X. Z. Organic photovoltaics integrated with thermoelectric generator achieving low critical temperature difference and efficient energy conversion. *Adv. Funct. Mater.* **2022**, *32*, 2109410.

[8] Liu, J.; Li, D. G.; Ma, W. Z.; Chen, Y. S.; Dou, C.; Meng, D.; He, Q. Y.; Li, X. Y.; Deng, X. C.; Cai, H. Y. All-day uninterrupted thermoelectric generator by simultaneous harvesting of solar heating and radiative cooling. *Opt. Express* **2023**, *31*, 14495–14508.
[9] Contento, G.; Lorenzi, B.; Rizzo, A.; Narducci, D. Efficiency enhancement of a-Si and CZTS solar cells using different thermoelectric hybridization strategies. *Energy* **2017**, *131*, 230–238.
[10] Suarez, F.; Nozariasbmarz, A.; Vashaee, D.; Öztürk, M. C. Designing thermoelectric generators for self-powered wearable electronics. *Energy Environ. Sci.* **2016**, *9*, 2099–2113.
[11] Twaha, S.; Zhu, J.; Yan, Y. Y.; Li, B. A comprehensive review of thermoelectric technology: Materials, applications, modelling and performance improvement. *Renew. Sustain. Energy Rev.* **2016**, *65*, 698–726.
[12] Miao, Z.; Meng, X. N.; Liu, L. Analyzing and optimizing the power generation performance of thermoelectric generators based on an industrial environment. *J. Power Sources* **2022**, *541*, 231699.
[13] Yang, Z. N.; Wang, F. Q.; Fu, Z. C.; Dong, Y.; Zou, H. C.; Chen, X. D.; Yan, Y. Y.; Zhang, S. Thermoelectric system investigation with the combination of solar concentration, greenhouse and radiative cooling for all-day power generation. *Renew. Energy* **2024**, *231*, 120903.
[14] Khan, S.; Kim, J.; Roh, K.; Park, G.; Kim, W. High power density of radiative-cooled compact thermoelectric generator based on body heat harvesting. *Nano Energy* **2021**, *87*, 106180.
[15] Ochieng, A. O.; Megahed, T. F.; Ookawara, S.; Hassan, H. Comprehensive review in waste heat recovery in different thermal energy-consuming processes using thermoelectric generators for electrical power generation. *Process Saf. Environ. Prot.* **2022**, *162*, 134–154.
[16] Jabri, M.; Masoumi, S.; Kandukuri, T. R.; Occhipinti, L. G. Flexible thin-film thermoelectric generators for human skin-heat harvesting: A numerical study. *Nano Energy* **2024**, *129*, 110001.
[17] Kraemer, D.; Jie, Q.; McEnaney, K.; Cao, F.; Liu, W. S.; Weinstein, L. A.; Loomis, J.; Ren, Z. F.; Chen, G. Concentrating solar thermoelectric generators with a peak efficiency of 7.4%. *Nat. Energy* **2016**, *1*, 16153.
[18] Xie, H. P.; Gao, T. Y.; Long, X. T.; Sun, L. C.; Wang, J.; Xia, E. T.; Li, S. H.; Li, B.; Li, C. B.; Gao, M. Z. et al. Design and performance of a modular 1 kilowatt-level thermoelectric generator for geothermal application at medium-low temperature. *Energy Convers. Manage.* **2023**, *298*, 117782.
[19] Khatirzad, H.; Sheikholeslami, M. Numerical investigation of hybrid nanofluid flow in a finned heat sink integrated with a concentrated solar system and thermoelectric generator. *Renew. Energy* **2025**, *245*, 122783.
[20] Raman, A. P.; Anoma, M. A.; Zhu, L. X.; Rephaeli, E.; Fan, S. H. Passive radiative cooling below ambient air temperature under direct sunlight. *Nature* **2014**, *515*, 540–544.
[21] Mandal, J.; Fu, Y. K.; Overvig, A. C.; Jia, M. X.; Sun, K. R.; Shi, N. N.; Zhou, H.; Xiao, X. H.; Yu, N. F.; Yang, Y. Hierarchically porous polymer coatings for highly efficient passive daytime radiative cooling. *Science* **2018**, *362*, 315–319.
[22] Wu, X. K.; Li, J. L.; Jiang, Q. Y.; Zhang, W. S.; Wang, B. S.; Li, R.; Zhao, S. M.; Wang, F.; Huang, Y.; Lyu, P. et al. An all-weather radiative human body cooling textile. *Nat. Sustain.* **2023**, *6*, 1446–1454.
[23] Mu, E. Z.; Wu, Z. H.; Wu, Z. M.; Chen, X.; Liu, Y.; Fu, X. C.; Hu, Z. Y. A novel self-powering ultrathin TEG device based on micro/nano emitter for radiative cooling. *Nano Energy* **2019**, *55*, 494–500.
[24] Raman, A. P.; Li, W.; Fan, S. H. Generating light from darkness. *Joule* **2019**, *3*, 2679–2686.
[25] Fan, L. L.; Li, W.; Jin, W. L.; Orenstein, M.; Fan, S. H. Maximal nighttime electrical power generation via optimal radiative cooling. *Opt. Express* **2020**, *28*, 25460–25470.
[26] Zhao, B.; Pei, G.; Raman, A. P. Modeling and optimization of radiative cooling based thermoelectric generators. *Appl. Phys. Lett.* **2020**, *117*, 163903.
[27] Deasy, M. J.; Baudin, N.; O'Shaughnessy, S. M.; Robinson, A. J. Simulation-driven design of a passive liquid cooling system for a thermoelectric generator. *Appl. Energy* **2017**, *205*, 499–510.
[28] Liu, J. W.; Zhang, J.; Yuan, J. J.; Zhang, D. B.; Xing, J. C.; Zhou, Z. H. Model development and performance evaluation of thermoelectric and radiative cooling module to achieve all-day power generation. *Sol. Energy Mater. Sol. Cells* **2021**, *220*, 110855.
[29] Wang, C. H.; Chen, H.; Jiang, Z. Y.; Zhang, X. X.; Wang, F. Q. Modelling and performance evaluation of a novel passive thermoelectric system based on radiative cooling and solar heating for 24-hour power-generation. *Appl. Energy* **2023**, *331*, 120425.
[30] Brunner, R.; Sandfuchs, O.; Pacholski, C.; Morhard, C.; Spatz, J. Lessons from nature: Biomimetic subwavelength structures for high‐performance optics. *Laser Photonics Rev.* **2012**, *6*, 641–659.
[31] Lotz, M.; Needham, J.; Jakobsen, M. H.; Taboryski, R. Nanoimprinting reflow modified moth-eye structures in chalcogenide glass for enhanced broadband antireflection in the mid-infrared. *Opt. Lett.* **2019**, *44*, 4383–4386.
[32] Guo, J. F.; Huai, X. L. Maximizing electric power through spectral-splitting photovoltaic-thermoelectric hybrid system integrated with radiative cooling. *Adv. Sci.* **2023**, *10*, 2206575.
[33] Zhang, W. W.; Guo, Y. M.; He, M. J.; Ren, Y. T.; Gao, B. H.; Qi, H. Self-adaptive photothermal/radiative cooling-thermoelectric conversion system for 24 h electricity generation. *Appl. Therm. Eng.* **2024**, *243*, 122603.
[34] Ding, Z. M.; Pattelli, L.; Xu, H. B.; Sun, W. H.; Li, X.; Pan, L.; Zhao, J. P.; Wang, C. Y.; Zhang, X.; Song, Y. et al. Iridescent daytime radiative cooling with no absorption peaks in the visible range. *Small* **2022**, *18*, 2202400.
[35] Zhu, X. Y.; Yu, Y.; Li, F. A review on thermoelectric energy harvesting from asphalt pavement: Configuration, performance and future. *Constr. Build. Mater.* **2019**, *228*, 116818.
[36] Kraemer, D.; Poudel, B.; Feng, H. P.; Caylor, J. C.; Yu, B.; Yan, X.; Ma, Y.; Wang, X. W.; Wang, D. Z.; Muto, A. et al. High-performance flat-panel solar thermoelectric generators with high thermal concentration. *Nat. Mater.* **2011**, *10*, 532–538.
[37] Baranowski, L. L.; Snyder, G. J.; Toberer, E. S. Concentrated solar thermoelectric generators. *Energy Environ. Sci.* **2012**, *5*, 9055–9067.
[38] Lekbir, A.; Hassani, S.; Ab Ghani, M. R.; Gan, C. K.; Mekhilef, S.; Saidur, R. Improved energy conversion performance of a novel design of concentrated photovoltaic system combined with thermoelectric generator with advance cooling system. *Energy Convers. Manage.* **2018**, *177*, 19–29.
[39] Ding, Z. M.; Li, X.; Zhang, H. L.; Yan, D. K.; Werlé, J.; Song, Y.; Pattelli, L.; Zhao, J. P.; Xu, H. B.; Li, Y. Robust radiative cooling via surface phonon coupling-enhanced emissivity from SiO_2 micropillar arrays. *Int. J. Heat Mass Transfer* **2024**, *220*, 125004.
[40] Xia, Z. L.; Zhang, Z. F.; Meng, Z. H.; Ding, L. Y.; Yu, Z. Q. Thermoelectric generator using space cold source. *ACS Appl. Mater. Interfaces* **2019**, *11*, 33941–33945.